LETTER

https://doi.org/10.1038/s41586-018-0861-0

Real-time vibrations of a carbon nanotube

Arthur W. Barnard[1,2,6,9], Mian Zhang[1,3,7,9], Gustavo S. Wiederhecker[3,4], Michal Lipson[3,5,8]* & Paul L. McEuen[2,5]*

The field of miniature mechanical oscillators is rapidly evolving, with emerging applications including signal processing, biological detection[1] and fundamental tests of quantum mechanics[2]. As the dimensions of a mechanical oscillator shrink to the molecular scale, such as in a carbon nanotube resonator[3–7], their vibrations become increasingly coupled and strongly interacting[8,9] until even weak thermal fluctuations could make the oscillator nonlinear[10–13]. The mechanics at this scale possesses rich dynamics, unexplored because an efficient way of detecting the motion in real time is lacking. Here we directly measure the thermal vibrations of a carbon nanotube in real time using a high-finesse micrometre-scale silicon nitride optical cavity as a sensitive photonic microscope. With the high displacement sensitivity of 700 fm $Hz^{-1/2}$ and the fine time resolution of this technique, we were able to discover a realm of dynamics undetected by previous time-averaged measurements and a room-temperature coherence that is nearly three orders of magnitude longer than previously reported. We find that the discrepancy in the coherence stems from long-time non-equilibrium dynamics, analogous to the Fermi–Pasta–Ulam–Tsingou recurrence seen in nonlinear systems[14]. Our data unveil the emergence of a weakly chaotic mechanical breather[15], in which vibrational energy is recurrently shared among several resonance modes—dynamics that we are able to reproduce using a simple numerical model. These experiments open up the study of nonlinear mechanical systems in the Brownian limit (that is, when a system is driven solely by thermal fluctuations) and present an integrated, sensitive, high-bandwidth nanophotonic interface for carbon nanotube resonators.

Measuring real-time dynamics is crucial for uncovering the distinct mechanics of a carbon nanotube (CNT)—a molecular-sized nanomechanical oscillator. However, this has not yet been demonstrated, owing to the CNT's extremely small size and its miniscule, yet fast, mechanical vibrations. Electrical techniques have limited bandwidth owing to large parasitic capacitive or inductive couplings. Electron microscopes have high spatial resolution but are invasive, produce unwanted material deposition on CNTs at room temperature, and are impractical for applications[16]. Using light is a promising approach, but is limited by the incredibly small optical cross-section of a CNT—most light passes the CNT without interacting with it[3,9,17,18]. Preliminary work coupling CNTs with optical fibre cavities[19], microwave cavities[20] and low-quality-factor (Q) microcavity resonators[21] have shown promise in improving optical coupling strength, but have not yet reached the level necessary to access the real-time dynamics of CNTs.

Here we show that coupling a nanometre-scale freestanding CNT to a high-Q micrometre-scale optical cavity can greatly enhance the effective optical cross-section and realize real-time measurements. We achieve enhanced optical coupling by using a pair of electrically contacted gold microtweezers (Fig. 1a) to suspend and position a single CNT less than a hundred nanometres away from an optical microcavity. Typical individual CNTs are 2–5 nm in diameter[22], 5–15 μm in length, and are held to the microtweezers by van der Waals attraction. The microtweezers are used to bring the CNTs from a chip coated with aligned CNTs to the fabricated optical microcavity. Conductance measurements confirm that a single CNT is held by the microtweezers. The relatively long CNT length when compared to the size of the optical mode ensures that when they are in the cavity nearfield, the tweezers do not perturb the optical cavity field (inset to Fig. 1b, Extended Data Fig. 1).

The optical microcavity has high-Q and small mode volume with substantial optical density in its evanescent field. We achieve this by designing and fabricating silicon nitride (Si_3N_4) free-standing microdisks 15 μm in radius and 320 nm in thickness[23] that typically exhibit loaded optical quality factors of about 1.5 million. Light at wavelength 1.59 μm is coupled in and out of the optical cavity through a tapered optical fibre and the optical transmission is monitored on a fast photodiode (Fig. 1b). The resulting configuration allows an electrically contacted CNT to be spatially controlled with high precision within the evanescent optical cavity field.

We first show that a single CNT residing in the optical-cavity nearfield strongly changes the optical transmission of the cavity. We monitor the optical cavity transmission while independently manoeuvring a CNT relative to the microdisk with a calibrated three-axis piezo positioner. As is commonly observed in high-Q optical cavities, minor defects break the degeneracy of the clockwise and counter-clockwise travelling wave optical modes and form two standing-wave optical modes that are spatially π out of phase and spectrally separate in resonance frequency (Fig. 2a, Extended Data Fig. 2). When the CNT is moved closer to the cavity, the linewidth of the optical transmission increases while the extinction decreases (Fig. 2a) owing to the absorption and scattering induced by the CNT. When the CNT is very close to the surface of the optical cavity, it snaps onto the cavity surface (probably owing to van der Waals attraction), as indicated by the sudden change of the transmission (Fig. 2a). The two standing-wave modes have distinct responses to the CNT owing to the difference in spatial overlap of the CNT and the two optical modes (Supplementary Discussion 1).

The high-finesse cavity increases the CNT–optical interaction strength by several orders of magnitude compared with free-space optics. We directly extract the absorption and scattering optical cross-section of the single CNT by measuring the shift in cavity resonant frequency and damping as the CNT shifts in position. As the CNT is brought into contact with the top surface of the cavity, the optical resonance linewidth ($\kappa/(2\pi)$, where κ is the optical cavity loss rate) changes from 120 MHz in the far-field to 400 MHz, with the CNT in contact with the microdisk. This demonstrates that the CNT can absorb as much as 50% of the light launched into the cavity. At the same time, we observe a cavity frequency shift of $\delta f = 100$ MHz caused by the refraction of the cavity field by the CNT. We apply cavity perturbation theory[24,25] and directly ascertain the absorption cross-section $d_{abs} = 100$ pm and the Rayleigh scattering length $d_{scatter} = 2$ pm (Extended Data Fig. 3, Supplementary Discussions 3, 9 and 10). These measurements are consistent with a CNT of diameter approximately 2 nm when compared with previous studies[26–28].

[1]School of Applied and Engineering Physics, Cornell University, Ithaca, NY, USA. [2]Laboratory of Atomic and Solid State Physics, Cornell University, Ithaca, NY, USA. [3]School of Electrical and Computer Engineering, Cornell University, Ithaca, NY, USA. [4]Gleb Wataghin Physics Institute, University of Campinas, Campinas, Brazil. [5]Kavli Institute at Cornell for Nanoscale Science, Cornell University, Ithaca, NY, USA. [6]Present address: Physics Department, Stanford University, Stanford, CA, USA. [7]Present address: John A. Paulson School of Engineering and Applied Sciences, Harvard University, Cambridge, MA, USA. [8]Present address: Electrical Engineering, Columbia University, New York, NY, USA. [9]These authors contributed equally: Arthur W. Barnard, Mian Zhang. *e-mail: ml3754@columbia.edu; plm23@cornell.edu

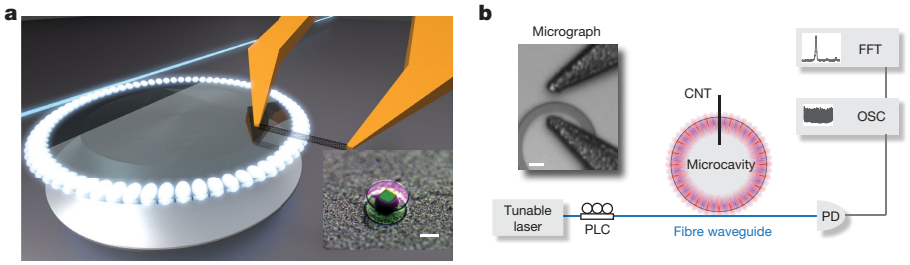

Fig. 1 | CNT–microcavity system. a, Schematic showing a CNT positioned over an optical microcavity with a pair of electrically contacted microtweezers. The optical cavity is excited by an optical tapered fibre waveguide. The CNT interacts with the evanescent optical field. The inset is an optical micrograph of a freestanding high-Q silicon nitride optical cavity. **b**, A tunable laser is used to excite the optical cavity and the optical transmission is recorded on a photodiode (PD). The presence of the CNT in the optical field induces a change in the optical transmission, which is recorded by an oscilloscope and analysed through a fast Fourier transform (FFT) algorithm. Scale bars, 10 μm.

The interaction strength of the CNT mechanical degree of freedom with the optical field is characterized by the (mainly dissipative) optomechanical coupling rate $g_k = \mathrm{d}\kappa/\mathrm{d}z$, where z is the CNT's vertical displacement. As expected for the profile of the cavity's evanescent field, the increase in the value of g_k with the shrinking of the CNT–cavity gap follows an exponential trend (Fig. 2b), yielding a fitted decay length of the evanescent field of 103 nm, in good agreement with simulations (Supplementary Discussion 2).

To probe the thermal Brownian vibrations of the CNT in real time, we simply measure the time-dependent intensity of the light transmitted through the optical microcavity as the nanotube vibrates in the evanescent field. For the data in Fig. 2c, the CNT is directly suspended on top of an antinode of a cavity standing wave created using 10 μW of continuous-wave laser power centred at the optical resonant frequency. We find unambiguous oscillatory signals in the optical transmission (Fig. 2c) at a frequency $f \approx 700$ kHz corresponding to the thermal, or Brownian, motion of the CNT. This signal is observable even when the CNT is relatively far away from the cavity (about 300 nm in Fig. 2c).

These real-time measurements reveal surprising behaviour, including a mechanical quality factor of 4,000–20,000 at room temperature, more than two orders of magnitude higher than that obtained by traditional measurement techniques. Positioning the CNT closer to the cavity to achieve optimal detection efficiency, in Fig. 3a we plot the broadband readout signal (50 kHz to 2 MHz) at several different timescales, where each plot is roughly 5.5 times longer than the previous one. Dominant oscillations of period 1.5 μs are clearly observed, and the amplitude of these oscillations are relatively constant on 0.5-ms timescales but vary in complex ways for larger times (Fig. 3a, b). The calibrated root-mean-squared vibration amplitude of the oscillations is $z_{\mathrm{th}} = 14$ nm, corresponding to a spring constant $k = k_{\mathrm{B}}T/z_{\mathrm{th}}^2 = 2 \times 10^{-5}$ N m^{-1} and a CNT of mass $m = k/\omega^2 = 1.5$ fg, indicating a diameter of less than 7 nm (Supplementary Discussion 12).

We use wavelet techniques to focus on the time-dynamics of the prominent resonance feature. We transform the time trace from Fig. 3b into a spectrogram and plot the results in Fig. 3c, where the colour map corresponds to instantaneous amplitude (audio representation in Supplementary Video 1). Several surprising features emerge. First, there are large variations in the resonant frequency, much larger than the short-timescale linewidth. Second, the frequency variations show a correlation with the oscillation amplitude, with larger amplitudes correlating with decreased frequency. Finally, and most surprisingly, these frequency/amplitude variations show pseudo-periodic behaviour with a period of around 10 ms. This is over 6,000 times longer than the bare oscillation period. These behaviours are profoundly different from expectations based on that of a simple linear resonator with a single loss rate and quality factor.

The pseudo-periodicity is completely unexpected, given previous narrow-band measurements. To demonstrate this, we integrate over

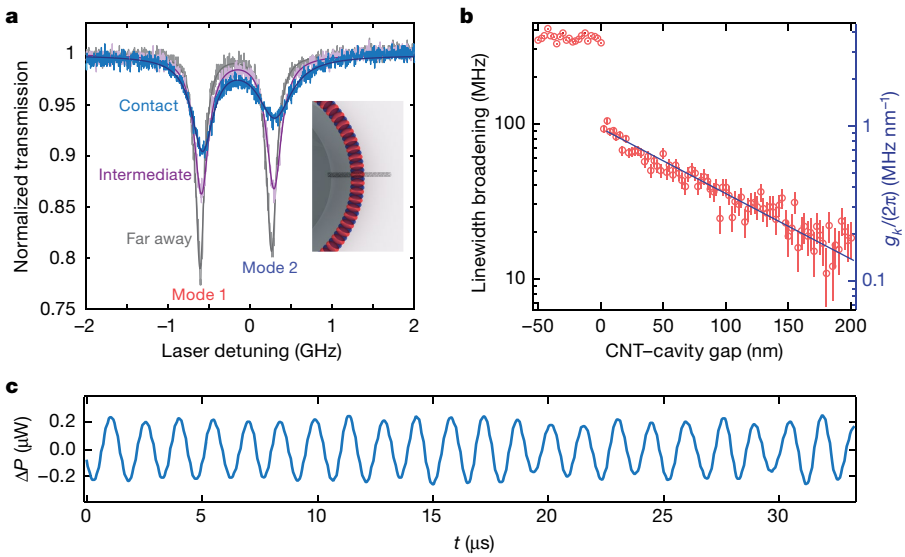

Fig. 2 | Characterizing the interaction between an optical microcavity and a single CNT. a, Optical cavity transmission with (blue) and without (grey) a CNT placed on the top surface of the optical cavity, illustrating the strong effect of the CNT on the cavity optical properties. The two modes are due to typical optical imperfections in the cavity that split the clockwise and counter-clockwise optical modes (shown as mode 1 and mode 2, illustrated in the inset). The purple trace illustrates an intermediate step, with the CNT still fully suspended. **b**, The measured linewidth broadening of a resonance (left) and its derivative ($g_k/(2\pi)$; right) as a function of gap width between the CNT and the optical cavity, illustrating the exponential variation of the coupling and the snap to contact. Error bars indicate the uncertainty in the linewidth fitting. **c**, Measured optical power variation due to CNT thermal vibration when the CNT is about 300 nm away from contact.

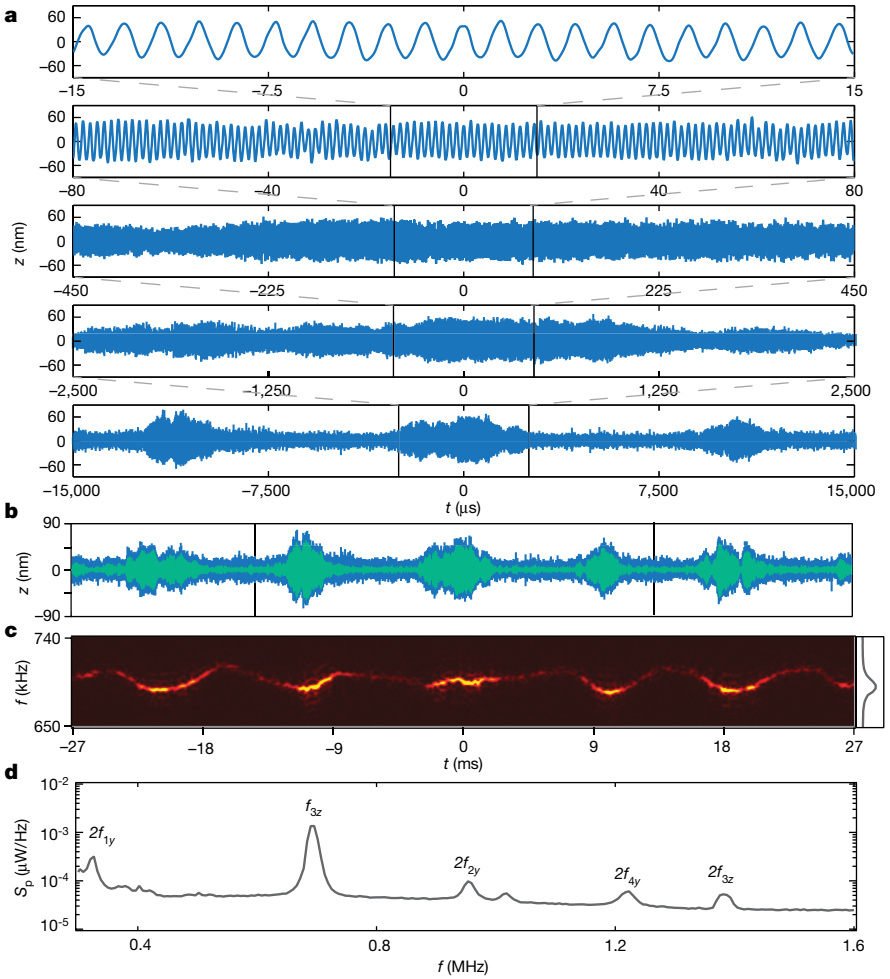

Fig. 3 | Time-domain measurement of CNT resonance. a, Broadband optical readout of thermal Brownian motion of the CNT at various timescales. Five different timescales are shown; vertical lines indicate the bounds of the previous plot. **b**, Longer-timescale plot with broadband signal (blue) and a phase-locked loop filtered signal (42-kHz bandwidth) around the dominant resonance feature (green), showing the presence of amplitude fluctuations. **c**, Wavelet transform of the time trace, revealing pseudo-periodic amplitude and frequency variations. The power spectral density of the resonance mode is plotted on the right, showing the apparently low Q_m that steady-state detection implies. **d**, Full power spectral density S_p with 600-Hz bandwidth computed by Fourier analysis from a 250-ms single-shot measurement. The signal-to-noise ratio is about 900, and we label resonance modes by matching spectral features to predictions for doubly clamped CNTs (Supplementary Discussion 6).

the time axis of the full spectrogram in Fig. 3c to calculate the power spectral density (inset to Fig. 3c and Fig. 3d). A series of broad peaks are observed, with the dominant one being the 700-kHz resonance. The full-width at half-maximum $\Delta f \approx 20$ kHz of the peak produces a $Q_m = f/\Delta f$ of about 35, consistent with previous results for CNT mechanical resonators measured at room temperature[3,19]. The complex spectral dynamics and the long energy relaxation times are completely hidden.

To categorize the mechanical dissipation rates from our broadband measurements, we first calculate the autocorrelation function $g_z(t)$ of the data in Fig. 3. This correlation function reflects both phase and amplitude variations in the signal and is shown in blue in Fig. 4a. It falls off with a characteristic timescale of around 50 μs, indicating a correlation quality factor of $Q_c \approx 40$.

We compute the amplitude envelope autocorrelation function $g_{AZ}(t)$ (purple, Fig. 4a) to detemine the time-dependent energy dissipation of the CNT. $g_{AZ}(t)$ is insensitive to frequency/phase variations and reflects only the mechanical energy loss rate. The measured data show that it falls off on millisecond times, then exhibits quasi-periodic modulations with a remarkably long decay time. Using the initial decay of $g_{AZ}(t)$, the mechanical quality factor $Q_m = \pi f \tau$ is around 4,000, where τ is the correlation time. However, the coherence of the overall system is clearly longer than this because the correlation function oscillates, indicating that energy coherently sloshes in and out of the mode. The decay of this oscillating signal indicates an overall system energy-loss quality factor of $Q_{sys} \approx 20{,}000$ (about 10 ms decay of the envelope in Fig. 4a).

Fermi, Pasta, Ulam and Tsingou (FPUT)[14] performed numerical simulations that showed that nonlinear strings, rather than equilibrating, can undergo slow periodic recurrences. This challenged the ergodicity hypothesis in statistical mechanics and inspired the genesis of several fields such as chaos and soliton theory[8,29,30]. Intuitively, an excited vibrational mode will approach thermal equilibrium over time by coupling to other degrees of freedom, leading all the modes to have energy $k_B T/2$. However, owing to strong nonlinear interactions, the ergodic condition can break down and complex pseudo-periodic behaviour can arise.

We show that the CNT Brownian pseudo-periodicity is FPUT-like and marks the emergence of a weakly chaotic mechanical breather[15]—energy concentrates in low-frequency modes, disperses into higher-frequency modes, and then returns. By using numerical simulations (Fig. 4b, d–h), we reproduce the spectro-temporal features of the pseudo-periodicity with remarkable similarity over a high bandwidth (Fig. 4d). Our simulations computed the time dynamics of a discrete-segment model of a thermalized, dissipationless CNT with boundary conditions consistent with our measurement (Supplementary Discussion 6). In the simulation, the fundamental in-plane mode (3z) has localized vibrational amplitude near the centre of the tube, which is

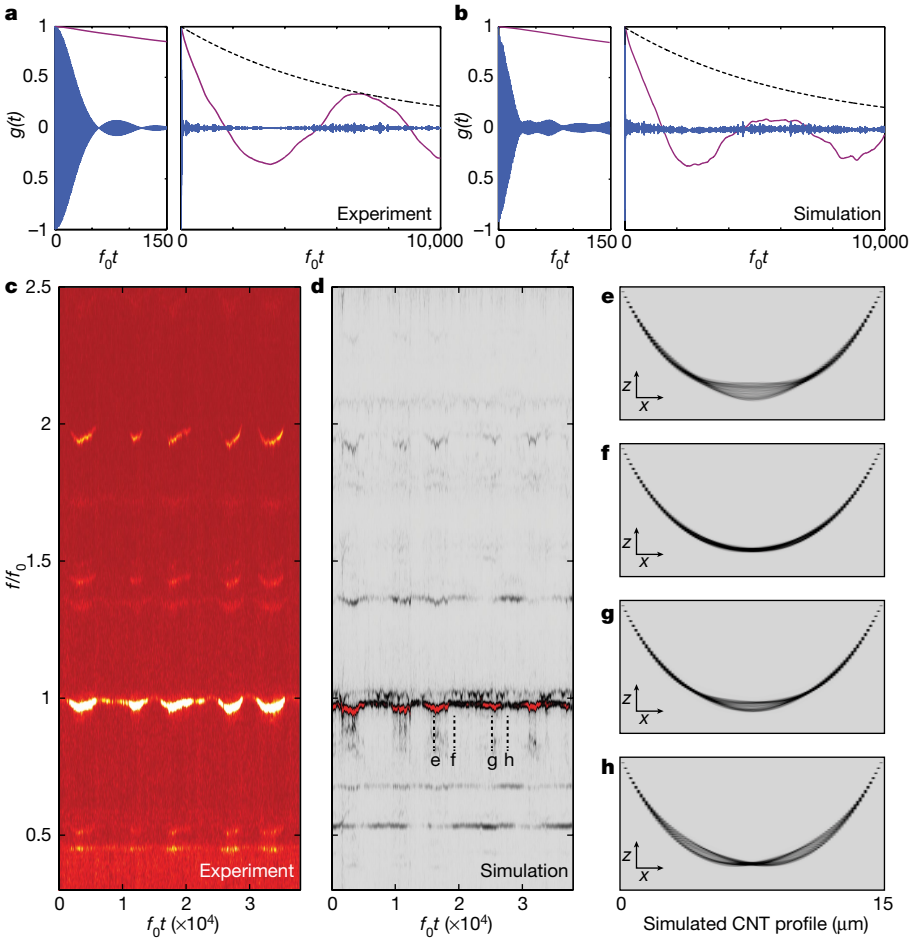

Fig. 4 | Spectral diffusion and mechanical breathers in the Brownian limit. a, Correlation functions of experimental data (extended from Fig. 3). The function $g_z(t)$ is the autocorrelation (blue), $g_{AZ}(t)$ is the amplitude envelope correlation (purple) and $g_{sys}(t)$ is the amplitude correlation envelope (dotted). The timescale of $g_{sys}(t)$ shows a long lifetime of the coupled CNT vibration modes (high-Q_m). **b**, Correlation functions of simulation data depicted in **d**–**h**. **c**, Broadband spectrogram of measured CNT motion in units of the bare frequency $f_0 = 700$ kHz with stronger optical coupling than in Fig. 3. The spectral diffusion is observed across several modes and harmonics. **d**, Broadband spectrogram of simulated CNT motion, revealing pseudo-periodicity with behaviour similar to what is shown in **c** over multiple modes. Frequency and time are normalized by the 3z mode frequency (f_0). The simulated pseudo-periodicity continues for five cycles in the simulation with an effective repetition rate of around 100–135 Hz. **e**–**h**, Sequential snapshots of simulated thermal vibrations of a thermally isolated CNT with size and boundary conditions similar to those of our measured CNT (specific points in time are labelled in **d**). The z-axis is expanded 20× for clarity. In **e** and **g**, vibrational energy is localized in the 3z mode. In **f**, energy is transferred to high-frequency modes, whereas in **h** the energy is dispersed to the sides of the CNT, remaining in lower-frequency modes.

a consequence of the clamping conditions. Following a period of high amplitude in the 3z mode (Fig. 4e), we observe lower-displacement amplitudes across the entire CNT as the vibrational energy is transferred to high-frequency modes (Fig. 4f). In the next high-amplitude traverse, the CNT is again vibrating with large amplitude at the centre (Fig. 4g). After this, the mechanical vibration disperses towards the sides of the CNT, remaining in other lower-frequency resonance modes (Fig. 4h). The concentration of energy in the fundamental in-plane mode appears consistent among all high-amplitude traverses, whereas the modes to which the energy disperses depend on specific conditions: when the fundamental in-plane mode has a high amplitude, energy tends to disperse into high-frequency modes, but otherwise it is shared among low-frequency modes. These simulations exhibit the same periodic oscillation in the amplitude correlation function and predict a long correlation time, similar to what was observed in our real-time measurements (Fig. 4b).

These results show FPUT-like behaviour of a CNT in the thermodynamic limit. Specifically, we see amplitude correlations among several resonances and observe that phase noise and energy transfer stem primarily from coupling to other thermally occupied modes via mechanical nonlinearities, as has been suggested by recent theories and studies at high mechanical amplitudes[10,13,31] (Extended Data Fig. 4; see Supplementary Discussions 14 and 15 for details).

The real-time study of nonlinear systems in the Brownian limit enabled by our technique opens a window to a rich and largely unexplored regime of mechanics. It combines the low dissipation of macroscopic mechanical systems with the strong thermally induced mode coupling of semi-flexible polymers. Uncovering the underlying principles in such systems could redefine our understanding of both dissipation and frequency stability in nanomechanical systems[32], enable new classes of measurements and applications, and shed light on the complex, fast dynamics in molecular processes.

Online content

Any methods, additional references, Nature Research reporting summaries, source data, statements of data availability and associated accession codes are available at https://doi.org/10.1038/s41586-018-0861-0.

Received: 5 September 2017; Accepted: 14 November 2018;
Published online: 21 January 2019

1. Arlett, J. L., Myers, E. B. & Roukes, M. L. Comparative advantages of mechanical biosensors. *Nat. Nanotechnol.* **6**, 203–215 (2011).

2. Poot, M. & van der Zant, H. S. J. Mechanical systems in the quantum regime. *Phys. Rep*. **511**, 273–335 (2012).
3. Sazonova, V. et al. A tunable carbon nanotube electromechanical oscillator. *Nature* **431**, 284–287 (2004).
4. Jensen, K., Kim, K. & Zettl, A. An atomic-resolution nanomechanical mass sensor. *Nat. Nanotechnol*. **3**, 533–537 (2008).
5. Lassagne, B., Tarakanov, Y., Kinaret, J., Garcia-Sanchez, D. & Bachtold, A. Coupling mechanics to charge transport in carbon nanotube mechanical resonators. *Science* **325**, 1107–1110 (2009).
6. Poncharal, P., Wang, Z. L., Ugarte, D. & de Heer, W. A. Electrostatic deflections and electromechanical resonances of carbon nanotubes. *Science* **283**, 1513–1516 (1999).
7. Chaste, J. et al. A nanomechanical mass sensor with yoctogram resolution. *Nat. Nanotechnol*. **7**, 301–304 (2012).
8. Karabalin, R. B., Cross, M. C. & Roukes, M. L. Nonlinear dynamics and chaos in two coupled nanomechanical resonators. *Phys. Rev. B* **79**, 165309 (2009).
9. Castellanos-Gomez, A., Meerwaldt, H. B., Venstra, W. J., van der Zant, H. S. J. & Steele, G. A. Strong and tunable mode coupling in carbon nanotube resonators. *Phys. Rev. B* **86**, 041402 (2012).
10. Barnard, A. W., Sazonova, V., van der Zande, A. M. & McEuen, P. L. Fluctuation broadening in carbon nanotube resonators. *Proc. Natl Acad. Sci. USA* **109**, 19093–19096 (2012).
11. Greaney, P. A., Lani, G., Cicero, G. & Grossman, J. C. Anomalous dissipation in single-walled carbon nanotube resonators. *Nano Lett*. **9**, 3699–3703 (2009).
12. Eichler, A., Moser, J., Dykman, M. I. & Bachtold, A. Symmetry breaking in a mechanical resonator made from a carbon nanotube. *Nat. Commun*. **4**, 2843 (2013).
13. Maillet, O. et al. Nonlinear frequency transduction of nanomechanical Brownian motion. *Phys. Rev. B* **96**, 165434 (2017).
14. Fermi, E., Pasta, J. & Ulam, S. *Studies of nonlinear problems*. Report LA-1940 (Los Alamos Scientific Laboratory, 1955).
15. Flach, S., Ivanchenko, M. V. & Kanakov, O. I. *q*-breathers and the Fermi–Pasta–Ulam problem. *Phys. Rev. Lett*. **95**, 064102 (2005).
16. Tsioutsios, I., Tavernarakis, A., Osmond, J., Verlot, P. & Bachtold, A. Real-time measurement of nanotube resonator fluctuations in an electron microscope. *Nano Lett*. **17**, 1748–1755 (2017).
17. Meerwaldt, H. B., Johnston, S. R., van der Zant, H. S. J. & Steele, G. A. Submicrosecond-timescale readout of carbon nanotube mechanical motion. *Appl. Phys. Lett*. **103**, 053121 (2013).
18. Moser, J., Eichler, A., Güttinger, J., Dykman, M. I. & Bachtold, A. Nanotube mechanical resonators with quality factors of up to 5 million. *Nat. Nanotechnol*. **9**, 1007–1011 (2014).
19. Stapfner, S. et al. Cavity-enhanced optical detection of carbon nanotube Brownian motion. *Appl. Phys. Lett*. **102**, 151910 (2013).
20. Schneider, B. H., Etaki, S., van der Zant, H. S. J. & Steele, G. A. Coupling carbon nanotube mechanics to a superconducting circuit. *Sci. Rep*. **2**, 599 (2012).
21. Miura, R. et al. Ultralow mode-volume photonic crystal nanobeam cavities for high-efficiency coupling to individual carbon nanotube emitters. *Nat. Commun*. **5**, 5580 (2014).
22. Almaqwashi, A. A., Kevek, J. W., Burton, R. M., DeBorde, T. & Minot, E. D. Variable-force microscopy for advanced characterization of horizontally aligned carbon nanotubes. *Nanotechnology* **22**, 275717 (2011).
23. Barclay, P. E., Srinivasan, K., Painter, O., Lev, B. & Mabuchi, H. Integration of fiber-coupled high-*Q* SiN_x microdisks with atom chips. *Appl. Phys. Lett*. **89**, 131108 (2006).
24. Anetsberger, G. et al. Near-field cavity optomechanics with nanomechanical oscillators. *Nat. Phys*. **5**, 909–914 (2009).
25. Zhu, J. et al. On-chip single nanoparticle detection and sizing by mode splitting in an ultrahigh-*Q* microresonator. *Nat. Photon*. **4**, 46–49 (2010).
26. Joh, D. Y. et al. Single-walled carbon nanotubes as excitonic optical wires. *Nat. Nanotechnol*. **6**, 51–56 (2011).
27. Liu, K. et al. High-throughput optical imaging and spectroscopy of individual carbon nanotubes in devices. *Nat. Nanotechnol*. **8**, 917–922 (2013).
28. Liu, K. et al. Systematic determination of absolute absorption cross-section of individual carbon nanotubes. *Proc. Natl Acad. Sci. USA* **111**, 7564–7569 (2014).
29. Munteanu, L. & Donescu, S. in *Introduction to Soliton Theory: Applications to Mechanics* (ed. Van der Werwe, A.) 149–172 (Springer, Dordrecht, 2005).
30. Onorato, M., Vozella, L., Proment, D. & Lvov, Y. V. Route to thermalization in the α-Fermi–Pasta–Ulam system. *Proc. Natl Acad. Sci. USA* **112**, 4208–4213 (2015).
31. Güttinger, J. et al. Energy-dependent path of dissipation in nanomechanical resonators. *Nat. Nanotechnol*. **12**, 631–636 (2017).
32. Cleland, A. N. & Roukes, M. L. Noise processes in nanomechanical resonators. *J. Appl. Phys*. **92**, 2758–2769 (2002).

Acknowledgements We thank A. Bachtold for discussions. This work was supported in part by the National Science Foundation under grant number 0928552. It was also supported by the Cornell Center for Materials Research with funding from the NSF MRSEC programme (DMR-1719875) and funding from IGERT (DGE-0654193). This work was performed in part at the Cornell NanoScale Facility, a member of the National Nanotechnology Coordinated Infrastructure (NNCI), which is supported by the National Science Foundation (Grant ECCS-1542081). G.S.W. acknowledges FAPESP (grant 2012/17765-7) and CNPq for financial support in Brazil.

Author contributions A.W.B. and M.Z. conceived the experiment, designed and fabricated the devices and performed the measurements. A.W.B., M.Z. and G.S.W. performed data analysis. All authors contributed to the writing of the manuscript. M.L. and P.L.M. supervised the project.

Competing interests The authors declare no competing interests.

Additional information
Extended data is available for this paper at https://doi.org/10.1038/s41586-018-0861-0.
Supplementary information is available for this paper at https://doi.org/10.1038/s41586-018-0861-0.
Reprints and permissions information is available at http://www.nature.com/reprints.
Correspondence and requests for materials should be addressed to M.L. or P.L.M.
Publisher's note: Springer Nature remains neutral with regard to jurisdictional claims in published maps and institutional affiliations.

METHODS

Microtweezers. Microtweezers are fabricated using a three-step photolithography process followed by lift-off. On a Cr/Au-coated substrate, the tines and electrode contacts of the tweezers are lithographically defined and formed out of 3–5-μm-thick electroplated Au. Following this, an SU-8 frame about 150 μm thick is fabricated on top of the electrodes. Prior to developing, a hinge is formed between adjacent cantilevers using deep-ultraviolet light exposure across the gap between the two arms of the SU-8 frame. The final tweezers are lifted off in Cr etchant, rinsed and dried in air.

The tweezers are then installed in a home-built piezo-flexural holder that can open and close the tweezers by bending the flexible SU-8 base of the tweezers. Electrical contact is made with each electrode using soft copper spring contacts. This holder is then mounted on a commercial three-axis piezo scanner, permitting the tweezers to be manoeuvred near to an independent substrate.

Photonic microcavity and fibre coupler. A 350-nm-thick layer of high-stress, low-pressure chemical vapour deposition silicon nitride (Si_3N_4) is grown on a silicon wafer with 3 μm of thermal oxide (SiO_2). The disk and a fibre taper support pattern are then defined on the wafer by electron beam lithography. The pattern is then transferred onto the wafer through reactive-ion etching using CF_4 chemistry. Finally, the structure is partially released using a timed wet etching process in diluted hydrofluoric acid (HF). Before testing, the sample is cleaned in a piranha/HF dip cycle.

Light is coupled into the structure with a tapered optical fibre fabricated using the standard flame-pulling technique. We designed a fibre support cantilever structure near the disk so that small gaps between the fibre and the disks can be steadily maintained with the support friction.

CNT measurement protocol. The experiments consist of two steps: picking up the CNT and then coupling the CNT to the photonic cavity. Both steps are achieved in a single run inside a vacuum chamber. Both the CNT growth chip and the photonic cavity chip are placed on a common sample holder that can be coarsely positioned in three dimensions. The microtweezers and the tapered optical fibre are positioned close to each other while fine-positioners enable nanometre control over their relative placement. The growth chip is first placed under the microtweezer with the tapered optical fibre retracted to allow CNT pickup. After a CNT is picked up, the photonic cavity chip is moved under the microtweezers and the tapered optical fibre is moved between the microtweezer and the photonic cavity chip. The tapered fibre is then carefully positioned near the optical cavity to achieve the desired optical coupling. Finally, the microtweezers along with the attached CNT are moved down vertically while the optical transmission and the photocurrent in the CNT are constantly monitored. We often first observe finite photocurrent as the CNT is brought into the optical evanescent field.

Data collection and analysis. All real-time data were collected with a 16-bit digital oscilloscope with a 2.5-MHz Butterworth filter at the input. Any specified bandpass filtering is applied in postprocessing with a second-order digital Butterworth filter. All spectrograms plotted use a Morlet wavelet transformation[33].

Code availability. Finite-element time-domain simulation code is available from the corresponding author on request.

Data availability

The data that support the findings of this study are available from the corresponding author on reasonable request.

33. Goupillaud, P., Grossmann, A. & Morlet, J. Seismic signal analysis and discrimination. III. Cycle-octave and related transforms in seismic signal analysis. *Geoexploration* **23**, 85–102 (1984).

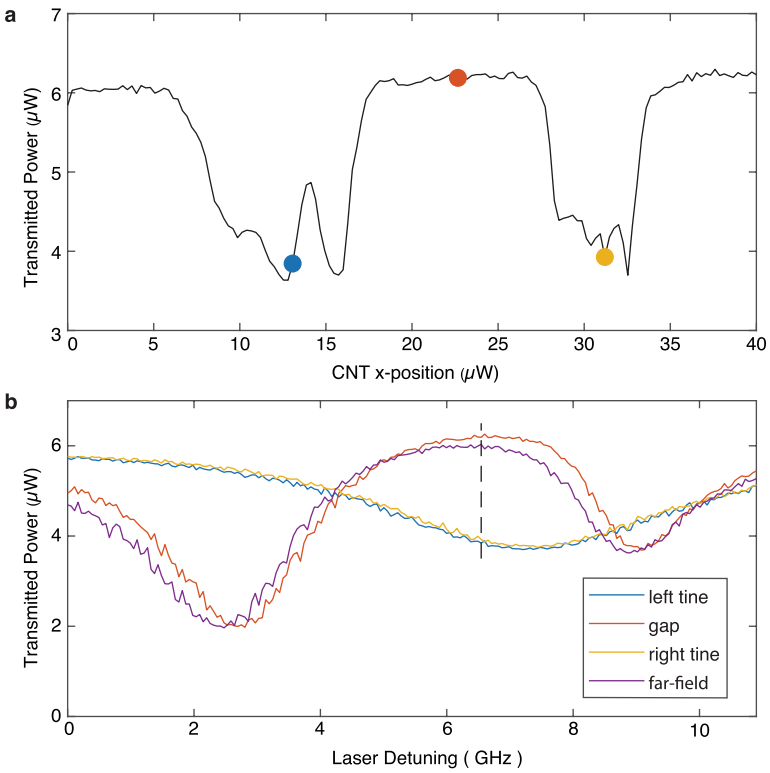

Extended Data Fig. 1 | Tweezer scattering. a, Spatial dependence of optical transmission at a fixed laser detuning as tweezers are scanned across the optical mode. Both tines (blue and yellow dots) are distinguishable and the gap region (orange dot) shows negligible perturbation. **b**, Cavity transmission spectra at select points in **a** along with a far-field spectrum. The dashed line corresponds to the fixed detuning used in **a**. The small differences in the gap spectrum and the far-field spectrum are attributed to slow thermal drifts between measurements.

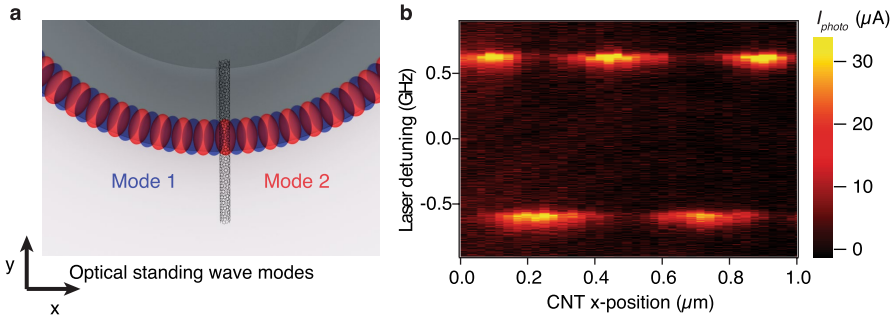

Extended Data Fig. 2 | Photocurrent mapping of the optical modes. **a**, Principle of the near-field photocurrent mapping of the cavity field. The suspended CNT is positioned close to the optical cavity and slowly scanned across the perimeter of the optical cavity. Modes 1 and 2 are two standing waves spatially π out of phase. **b**, Photocurrent signal (I_{photo}) from the CNT as the laser wavelength is rapidly swept across the two optical standing wave modes. The alternating photocurrent strength corresponds to the spatial geometry of the two optical standing waves.

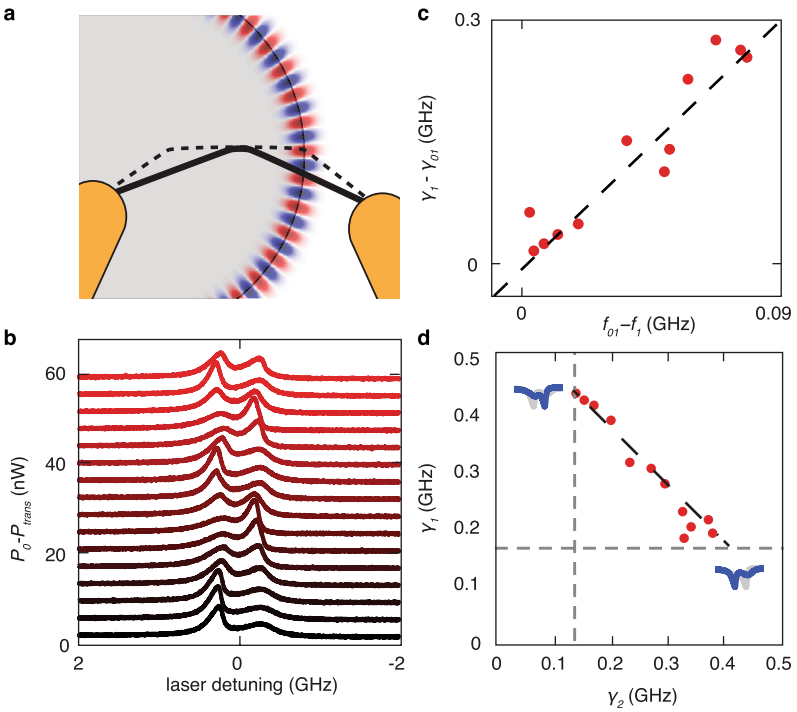

Extended Data Fig. 3 | Optical polarizability measurements. **a**, Schematic of the measurement. The CNT is touched to the surface of the cavity (dotted line) and then the tweezers are moved downward in the plane of the cavity, moving the CNT over several optical nodes. **b**, The resulting transmission data as a function of displacement (plotted from black to red). Resonance spectra are plotted as the difference between the off-resonance power (P_0) and the transmitted power (P_{trans}) and are displaced for clarity. **c**, Relationship between shifts in damping γ_1 and frequency f_1 (referenced to their respective far-field quantities γ_{01} and f_{01}) for the higher-frequency mode. **d**, Relationship between the damping rates of both cavities. Vertical and horizontal lines denote the far-field damping rates γ_{01} and γ_{02} respectively and the blue spectra correspond to the maximum damping condition for each mode. The linear fit specifies the maximum damping rate $\gamma \approx 450$ MHz and is due to the orthogonality of the two spatial modes.

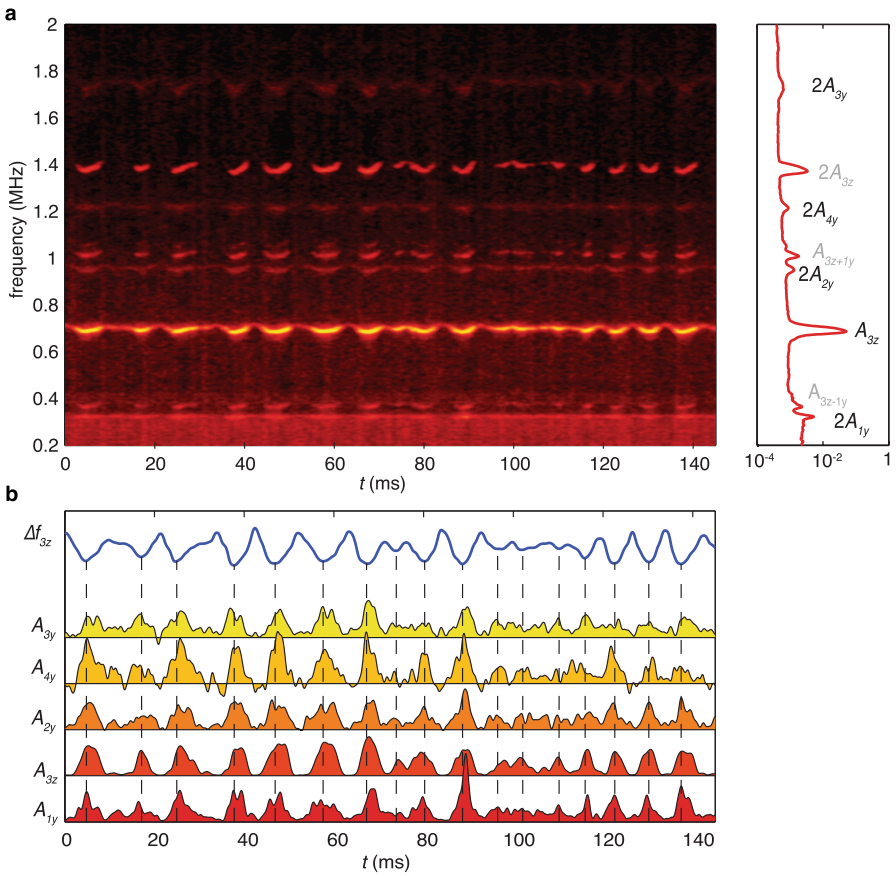

Extended Data Fig. 4 | Broadband analysis of pseudo-periodic resonances. a, Spectrogram of 145 ms of continuous data, revealing correlations of amplitude and frequency variation among several resonance modes. The power spectrum is plotted on the right with modes labelled based on analysis in Supplementary section 5. **b**, Correlations between resonance mode amplitudes A and frequency shifts Δf. The frequency shifts of f_{3z} is plotted above (blue), with dotted lines corresponding to local minima. The (normalized) amplitudes of five modes are plotted below.